Bioactive Materials 4 (2019) 312–321

Contents lists available at ScienceDirect

Bioactive Materials

journal homepage: http://www.keaipublishing.com/biomat

Multifunctional zinc ion doped sol – gel derived mesoporous bioactive glass nanoparticles for biomedical applications

Zuzana Neščáková[a,c], Kai Zheng[c], Liliana Liverani[c], Qaisar Nawaz[c], Dagmar Galusková[b], Hana Kaňková[b], Martin Michálek[a], Dušan Galusek[a,b], Aldo R. Boccaccini[c,*]

[a] Dept. of Biomaterials, FunGlass - Centre for Functional and Surface Functionalized Glass, Alexander Dubček University of Trenčín, Slovakia
[b] Central Laboratories, FunGlass - Centre for Functional and Surface Functionalized Glass, Alexander Dubček University of Trenčín, Slovakia
[c] Institute of Biomaterials, Department of Materials Science and Engineering, University of Erlangen, Nuremberg, Germany

ARTICLE INFO

Keywords:
Bioactive particles
Sol-gel synthesis
Zinc
Bioactivity
Ion release
Bioactive glass

ABSTRACT

Mesoporous bioactive glasses have been widely investigated for applications in bone tissue regeneration and, more recently, in soft tissue repair and wound healing. In this study we produced mesoporous bioactive glass nanoparticles (MBGNs) based on the SiO_2–CaO system. With the intention of adding subsidiary biological function, MBGNs were doped with Zn^{2+} ions. Zn-MBGNs with 8 mol% ZnO content were synthesized via microemulsion assisted sol-gel method. The synthesized particles were homogeneous in shape and size. They exhibited spherical shape, good dispersity, and a size of 130 ± 10 nm. The addition of zinc precursors did not affect the morphology of particles, while their specific surface area increased in comparison to MBGNs. The presence of Zn^{2+} ions inhibited the formation of hydroxycarbonate apatite (HCAp) on the particles after immersion in simulated body fluid (SBF). No formation of HCAp crystals on the surface of Zn-MBGNs could be observed after 14 days of immersion. Interestingly, powders containing relatively high amount of zinc released Zn^{2+} ions in low concentration (0.6–1.2 mg L^{-1}) but in a sustained manner. This releasing feature enables Zn-MBGNs to avoid potentially toxic levels of Zn^{2+} ions, indeed Zn-MBGNs were seen to improve the differentiation of osteoblast-like cells (MG-63). Additionally, Zn-MBGNs showed higher ability to adsorb proteins in comparison to MBGNs, which could indicate a favourable later attachment of cells. Due to their advantageous morphological and physiochemical properties, Zn-MBGNs show great potential as bioactive fillers or drug delivery systems in a variety of applications including bone regeneration and wound healing.

1. Introduction

Bioactive glasses (BGs) are attractive materials for bone tissue regeneration due to their ability to bond to bone, safely dissolve in the body and stimulate osteogenesis [1]. In the last decade, their application possibilities have broadened into the area of soft tissue engineering and wound healing [2–5]. The original melt-quenched BG, 45S5 Bioglass® [6], is nowadays prepared with many different modifications and numerous BG compositions are being continuously proposed and investigated [3,5,7]. Particularly, the relatively low-temperature sol-gel route allows to fabricate BGs of sophisticated structure (e.g., porous scaffolds, nanoparticles), to incorporate drugs and growth factors as well as to synthesize hybrid BGs [1,8,9]. The discovery of mesoporous bioactive glasses (MBGs) opened a new direction for developing multifunctional bioactive materials in regenerative medicine [10]. The main feature of MBGs is the presence of a mesoporous channel structure with pore size in the range 5–20 nm [11]. Compared to conventional BGs, MBGs offer significantly higher specific surface area, large pore volume and uniform pore size, which enable MBGs to be promising carrier platforms for delivery of drugs and biomolecules [12]. Moreover, in comparison to conventional micron-sized BGs, nanoscale MBGs exhibit characteristics of interaction with cells at the nanoscale and integration with the extracellular matrix to a greater extent [2,12,13]. MBGs can also incorporate a variety of therapeutics ions, such as Cu and Sr, to boost specific biological properties (e.g., angiogenesis, osteogenesis). Given their morphological and compositional advantages, MBGs are recognized as multifunctional materials, being able to provide osteogenesis, angiogenesis and anti-bacterial activity [3,14–17].

Among a large number of therapeutic ions, Zn^{2+} ions are attracting increasing attention for tissue engineering applications [15,16–18].

Peer review under responsibility of KeAi Communications Co., Ltd.
* Corresponding author.
E-mail address: aldo.boccaccini@fau.de (A.R. Boccaccini).

https://doi.org/10.1016/j.bioactmat.2019.10.002
Received 15 June 2019; Received in revised form 19 September 2019; Accepted 7 October 2019
Available online 27 October 2019

Zinc is known to play crucial roles in the formation, mineralization, development and maintenance of healthy bones [18]. Zn ions are also involved in homeostasis, angiogenesis and antibacterial action [17–20]. In addition, zinc acts as a cofactor in several transcription factors and enzymes [21]. Zinc is also strongly connected with wound healing processes by enhancing proliferation of fibroblasts, epithelial cells migration and reducing superinfection and necrosis [20,21,22]. Zn-containing MBG powders and scaffolds have been reported by using sol-gel based processes [16,17,22,23,24]. The incorporation of Zn has been reported to affect the textural characteristics (e.g., pore size, pore volume) and physiological properties (e.g., apatite forming ability, dissolution behaviour). Zn-containing nanoscale BGs have also been synthesized using sol-gel based approaches [25]. However, the dispersity and homogeneity in size and shape (important parameters when nanoparticles are considered for applications in drug delivery and composite fabrication), of these Zn-containing nanoscale BGs should be improved. Alternatively, Zn could also be incorporated into nanoscale BGs through post-modification [13], through which the dispersity and homogeneity of particles could be improved. However, the synthesis and applications of Zn-containing mesoporous bioactive glass nanoparticles (Zn-MBGNs) have been rarely reported, though these materials are particularly attractive in various biomedical applications including wound healing, bone regeneration, and drug delivery.

In this study, we report the synthesis of highly dispersed and homogenous Zn-MBGNs by using a microemulsion-assisted sol-gel approach. The physiochemical and structural properties of Zn-MBGNs were comprehensively investigated. The influence of Zn^{2+} doping on apatite forming ability, protein adsorption and cytotoxicity effects were evaluated and discussed.

2. Materials and methods

2.1. Synthesis of MBGNs

Zn-containing mesoporous bioactive glass nanoparticles (Zn-MBGNs) were synthesized by using a microemulsion-assisted sol-gel approach [26]. Briefly, 2.24 g hexadecyltrimethylammonium bromide (CTAB) was dissolved in 104 mL of deionized water under continuous stirring at 30 °C for 30 min. Then, 32 mL of ethyl acetate was slowly poured into the solution under continuous stirring for 30 min. Subsequently, ammonium hydroxide (28%) was added to maintain pH at 10.5. After 15 min 23.04 mL of tetraethyl orthosilicate (TEOS) was added to the mixture and stirred for 30 min. Afterwards 4.34 g of $Ca(NO_3)_2.4H_2O$ was added. After 30 min, 1.09 g $Zn(NO_3)_2.6H_2O$ was added into the solution. The nominal composition of Zn-MBGNs was 70SiO2–25CaO–5ZnO (mol%). The mixture was stirred further for 4 h and then the suspension was centrifuged at a rate 9000 rpm (Centrifuge 5430R, Eppendorf, Germany) for 10 min to separate particles from the mixture. The precipitate was then washed twice with water and once with ethanol. Subsequently, the precipitate was dried in an oven at 60 °C for 24 h, followed by calcination at 700 °C for 2 h at a heating rate of 2 °C min^{-1}. As a comparison, 70SiO2–30CaO MBGNs were synthesized using the same method. Instead of the addition of Zn^{2+} precursor, only 5.21 g of $Ca(NO_3)_2.4H_2O$ was added. All the used chemicals were purchased from Sigma-Aldrich (Darmstadt, Germany) without further purification.

2.2. Characterization of MBGNs

The morphology and qualitative compositional analysis were performed using scanning electron microscopy (Zeiss Auriga 4750) with an EDX detector (Bruker, Oxford Instruments). Samples were dispersed in ethanol and dropped onto aluminium stubs without further coatings. The particle size distribution was determined using ImageJ (NIH, USA).

The quantitative elementary analysis of prepared MBGNs was obtained using X-ray fluorescence spectroscopy (XRF; Bruker S8 Tiger) and optical emission spectroscopy with inductively coupled plasma (ICP-OES; Agilent 5100 SVDV).

Fourier transform infrared spectroscopy (FTIR; IRAffinity-1S spectrophotometer, SHIMADZU, Japan) was carried out in transmission mode at the wavenumber ranging from 4000 to 400 cm^{-1} at the scan speed 23 scan/min with a resolution of 4 cm^{-1}.

X-ray diffraction analyses (XRD) were performed using X-ray diffractometer (MiniFlex 600, Rigaku, USA) in the 2Θ range of 10°–60° equipped with Cu Kα radiation. A step size of 0.010° and dwell time of 1° per minute were used. Samples were dispersed on low background silicon wafer (Bruker, AXS) before measurement.

N_2 adsorption-desorption isotherms at 77 K, used to determine the surface area and pore size distribution, were performed in Quantachrome® ASiQwin™ gas adsorption analyser (Quantachrome Instruments, USA). Before the adsorption measurements, samples were degassed under vacuum for 12 h at 300 °C. The surface area was obtained by applying the Brunauer-Emmet-Teller method. The pore size was determined by the Barrett-Joyner-Halenda method.

2.3. In vitro bioactivity

For *in vitro* bioactivity testing, samples were immersed in simulated body fluid (SBF) and the formation of hydroxycarbonate apatite (HCAp) crystals on the surface was investigated. As proposed by Kokubo et al. [27], SBF is buffered at body pH and contains the inorganic constituents of human blood plasma in an attempt to simulate an *in vivo* environment. The *in vitro* mineralization of the glasses was examined by immersing them in freshly prepared SBF. The synthesized nanoparticles (20 mg) were pressed into pellets (d = 1.5 cm), which were soaked in 40 mL of SBF (pH 7.4) according to the equation Vs = Sa/10 (Vs: SBF volume in mL, Sa: external surface area of the disks in mm^2). The specific surface area of MBGNs was not considered. Disk were located in sterile containers and incubated under continuous agitation (120 rpm) at 37 °C for different time points (1, 3, 7 and 14 days). No refreshment or adjustment of the solution was performed. After each predetermined time point, SBF was removed and samples were gently rinsed with deionized water. Afterwards, samples were dried in an oven at 60 °C for 24 h. Characterization studies using SEM, FTIR and XRD were carried out to reveal the possible formation of hydroxycarbonate apatite (HCAp) at the surface of each sample.

2.4. Ion release in SBF

The ions released from the tested samples into SBF were measured, wherein 75 mg of each type of powders were soaked in 50 mL of SBF. Samples were incubated at 37 °C with an agitation speed of 120 rpm. At each predetermined time point the supernatant was sampled and concentrated HNO_3 was added to meet pH ≤ 2 in order to stabilize the solution containing the dissolved ions. All samples were analysed by optical emission spectroscopy with inductively coupled plasma (ICP-OES; Agilent 5100 SVDV). A series of four calibration solutions was prepared to obtain a linear correlation between intensity of ions and concentration. The reference standards certified for ICP techniques were diluted to prepare the stock calibration solutions. The internal standardization technique with scandium as internal standard, was used in order to deal with non-spectral interferences. Precision of the analysis for all required ions, expressed as RSD%, was below 5%. The average values including standard deviations from three replicates for each dissolved ion were reported. The time dependence of the cumulative concentrations of Si^{4+}, Ca^{2+} and Zn^{2+} released into SBF medium was analysed.

2.5. Protein adsorption

The protein adsorption capability of MBGNs or Zn-MBGNs was quantitatively evaluated using bicinchoninic acid (BCA; Thermo Fisher,

Germany) in a colorimetric detection assay. Briefly, the particles were soaked in bovine serum albumin (BSA; Sigma-Aldrich) solution (1 mg mL^{-1}) in ultra-pure water for 2 h or 4 h at 37 °C. At the predetermined time points, 50 μL of supernatants was collected and mixed with 1 mL of the working reagent (Pierce; Thermo Fisher, Germany). After further incubation for 30 min at 37 °C, the protein concentration in the supernatant was quantified by a UV-VIS spectrophotometer (Specord®40, Analytik Jena, Germany) at 532 nm. Adsorption values were calculated by subtracting the measured protein concentration in the supernatant from the initial protein concentration in the protein solution.

2.6. In vitro biocompatibility assay

In vitro cytocompatibility experiments were performed using human osteoblast like cells (MG-63) and mouse embryonic fibroblasts cells (MEFs). MG-63 and MEF cell lines were purchased from European Collection of Authenticated Cell Cultures (ECACCS, Sigma Aldrich, Darmstadt, Germany). Cell lines were maintained in Dulbecco's Modified Eagle Medium (Gibco®, Thermo Fisher Scientific, USA). All reagents were purchased from Thermo Fisher Scientific (USA). The cell culture was performed in a humidified atmosphere of 95% air and 5% CO_2 at 37 °C. Cell lines were routinely subcultured by trypsinization (0.25% Trypsin-EDTA, Gibco®, Thermo Fisher Scientific, USA).

Cytotoxicity to a specific cell type was evaluated by elution test method ISO 10993–5 [28]. In the elution test method, extracts were obtained by placing the test materials in separate cell culture media incubated for 24 h at 37 °C. Powders at concentration of 0.1 mg mL^{-1}, 1 mg mL^{-1} and 5 mg mL^{-1} were used. Cells without treatment with powders were used as a control. The obtained fluid extract was collected by centrifugation and without any solid residues was applied to a pre-cultured cell monolayer and jointly incubated for 2 days under CO_2 atmosphere at 37 °C. After the treatment, the medium was removed and cells were rinsed with phosphate buffered saline (PBS). Mitochondrial activity of the cells in contact with extract fluids was measured using WST-8 method (CCK-8 Kit, Sigma Aldrich, Germany). WST-8-(2-(2-methoxy-4-nitrophenyl)-3-(4-nitrophenyl)-5-(2,4-disulfophenyl)-2H-tetrazolium is bioreduced by cellular dehydrogenases to an orange formazan product. After incubation for 4 h at 37 °C, the reaction's product was measured at 450 nm using microplate reader (PHOmo Elisa reader, Autobio Diagnostics Co. Ltd., Zhengzhou, China). The amount of formazan produced is directly proportional to the number of living cells in culture. Relative cell viability was determined according to the equation:

Relative cell viability (%) = Sample (OD at 460 nm)/Control (OD at 460 nm) x 100%

2.7. Statistical analysis

All experiments were carried out at least in triplicate. Results are expressed as mean ± standard deviation (SD). Statistical evaluation was assessed using Student's test. A value of $p < 0.05$ was considered statistically significant.

3. Results

3.1. Morphology and structural characteristic of MBGNs

The morphology of the prepared particles was analysed by scanning electron microscopy (SEM). Fig. 1 (a – d) shows dispersed, spherical (ovoidal) particles with visible nanoporosity. The average particle size was in both cases in the range of 130 ± 10 nm. Dispersity of nanoparticles was reached by using the microemulsion assisted sol-gel method, which also explains the homogeneity in the size and shape of the obtained nanoparticles [29].

EDX spectra for MBGNs and Zn-MBGNs are shown in Fig. 2. The EDX spectrum of Zn-MBGNs clearly indicates the presence of Si, Ca and Zn (Fig. 2b) while only Si and Ca can be observed in the spectrum of MBGNs (Fig. 2a).

Table 1 summarizes the composition of prepared nanoparticles measured by XRF and ICP-OES. The molar percentages of oxides are expressed according to XRF and ICP-OES elementary analysis and considering that all the elements are in form of oxides. Because of the high content of SiO_2 and its potential lost during the decomposition process before ICP-OES analysis, SiO_2 values were considered to be 100%. As expected, only SiO_2 and CaO could be detected in MBGNs while additional Zn was found in Zn-MBGNs. The detected composition of particles using XRF and ICP-OES was not significantly different.

XRD spectra shown in Fig. 3a display similar patterns for MBGNs and Zn-MBGNs powders. A broad band in the range of 20°–34° (2Θ) could be ascribed to the amorphous silicate while no diffraction peaks could be observed in the XRD patterns indicating the amorphous nature of both samples. FTIR spectra (Fig. 3b) show no additional changes in the molecular structure after the addition of Zn. IR spectra demonstrated a wide band located between 1000 and 1250 cm^{-1}. This band composed of an intensive peak attributed to the transverse optical mode (TO1) of the Si–O–Si stretching vibration at 1090 cm^{-1}, a shoulder identified as a TO2 mode of the Si–O–Si stretching vibration at 1220 cm^{-1}. The characteristic band of the Si–O–Si wagging vibration at around 800 cm^{-1}, as well as a Si–O–Si rocking mode near 470 cm^{-1} were identified [28,29–31].

The textural properties of particles were characterised by nitrogen adsorption measurements. Fig. 4a displays type IV isotherms, which is a characteristic feature of mesoporous materials [11]. Fig. 4b shows pore size distribution, appearing similar for both tested powders. Specific values are summarized in Table 2. MBGNs have a slightly larger pore volume compared with Zn-MBGNs. The diameter of the pores is comparable for MBGNs and Zn-MBGNs. All results indicate that the incorporation of Zn did not significantly affect the morphology and structure of particles.

3.2. In vitro bioactivity

The morphology of synthesized nanoparticles after immersion in SBF was observed by SEM. Fig. 5 shows SEM images of MBGNs and Zn-MBGNs after immersion in SBF for 7 days. Fig. 5a shows the formation of needle-like shapes covering the MBGNs surface while such morphology could not be observed on Fig. 5b displaying Zn-MBGNs. The changes in elementary composition after immersion in SBF were detected by EDX (Fig. 6a and b) in which the presence of P was confirmed in both particles after immersion in SBF. The Ca/P ratio of the MBG surface was ~1.64, similar to the Ca/P ratio in HCAp. The pH of the solution was adjusted to 7.4 at the beginning of the immersion test. Since SBF was not refreshed or adjusted during the immersion process, the pH reached a value of 7.50 ± 0.03 (MBGNs) and 8.10 ± 0.02 (Zn-MBGNs) after 14 days of soaking.

XRD patterns confirm the formation of hydroxycarbonate apatite (HCAp) on the surface of nanoparticles upon immersion in SBF. As observed in Fig. 7, the behaviour of MBGNs and Zn-MBGNs was different. XRD patterns for MBGNs show a semi crystalline phase with main peak matching with HAp at 32° (2Θ) [32]. This peak starts to be visible after 3 days of immersion in SBF and became relatively more intense with prolonged immersion time. XRD spectra of zinc-doped Zn-MBGNs nanoparticles did not show any crystalline peak throughout the whole immersion period.

In vitro mineralization of the synthesized nanoparticles after soaking in SBF was also characterised by FTIR. Fig. 8 displays the differences between FTIR spectra for MBGNs (Fig. 8a) and Zn-MBGNs (Fig. 8b). Bands in a region of 1000–1100 cm^{-1} are associated with the stretching modes of the PO_4^{3-} bonds in HCAp and the band in the region of 600 cm^{-1} corresponds to amorphous calcium phosphate. The split of this band in two bands at 560 cm^{-1} and 603 cm^{-1} is indicative of

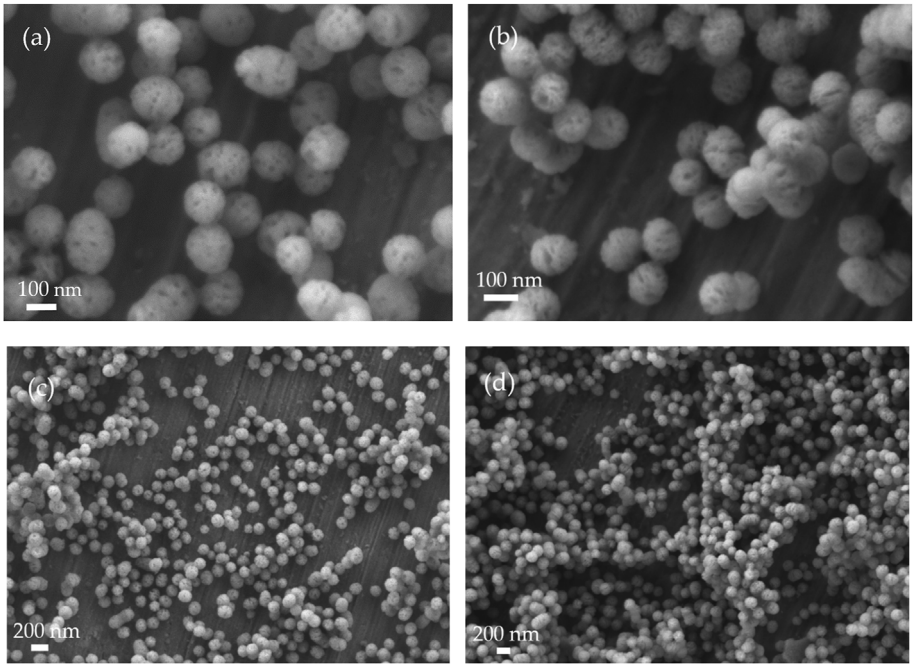

Fig. 1. Morphology of synthesized MBGNs (a, c) and Zn-MBGNs (b, d) particles obtained by SEM at different magnifications.

phosphate in a crystalline environment [33]. FTIR spectra of Zn-MBGNs nanoparticles did not show any of the above mentioned bands, even after 14 days of immersion.

3.3. Ion release

Release behaviour of Zn^{2+}, Ca^{2+} and Si^{4+} ions from MBGNs and Zn-MBGNs is shown in Fig. 9. Cumulative release of ions (mg L^{-1}) was measured upon immersion of powders in SBF for 14 days. The measured concentration of Zn^{2+} ions (Fig. 9a) was in the range 0.6–1.2 mg L^{-1}, this concentration slightly increased with time during the 14 day period of the test. Zn-MBGNs nanoparticles were able to release relatively low levels, but sustained amount of Zn^{2+} ions up to 14 days. A burst release of Ca^{2+} ions (Fig. 9b) by MBGNs was visible within 1 day (40 mg L^{-1}). From day 7, the level of Ca^{2+} ions is within the noise of the measured values of Ca^{2+} in SBF. Zn-MBGNs released Ca^{2+} ions in controlled manner and the highest amount was measured at the third day (20 mg L^{-1}). During the whole immersion period the level of Ca^{2+} ions was higher than the level present in SBF. MBGNs released Si^{4+} ions (Fig. 9c) faster (1 day - 70 mg L^{-1}) compared with Zn-MBGNs (1 day - 52 mg L^{-1}). The highest value for Si^{4+} ions released by Zn-MBGNs was

Table 1
X-ray fluorescence (XRF) and inductively coupled plasma optical emission spectroscopy (ICP-OES) were used to provide compositional analyses of MBGNs and Zn-MBGNs.

Composition XRF (mol %)	MBGNs	Zn-MBGNs
SiO_2	90.0	83.2
CaO	10.0	8.4
ZnO	–	8.4
Composition ICP-OES (mol %)		
SiO_2 (not measured)	88.4	83.8
CaO	11.6	8.3
ZnO		7.9

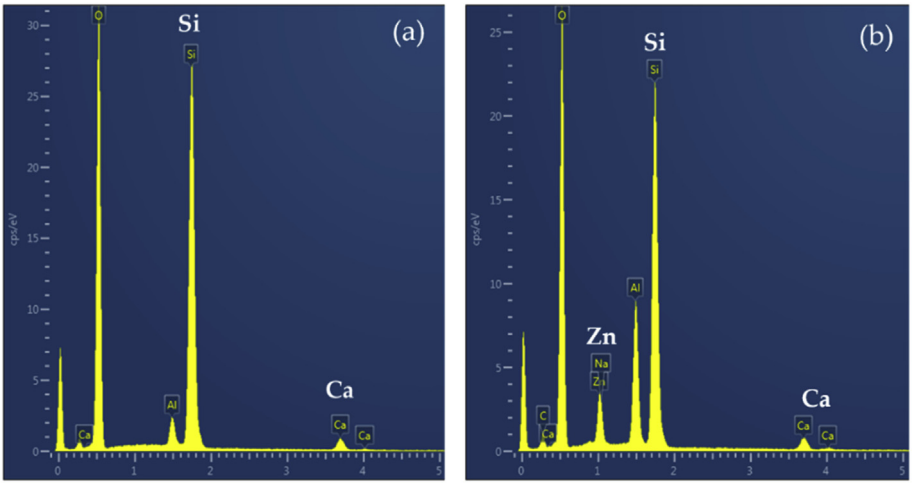

Fig. 2. Energy-dispersive x-ray spectroscopy (EDX) results for synthesized nanoparticles: (a) MBGNs and (b) Zn- MBGNs. The peaks assigned to Al were detected from the substrate.

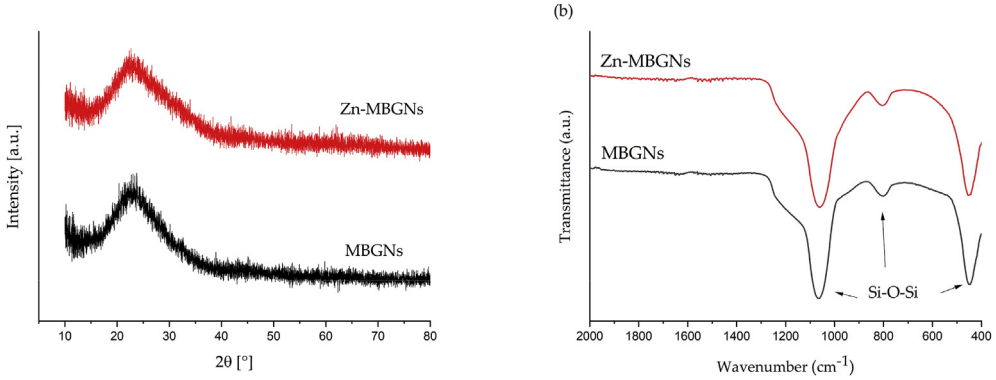

Fig. 3. X-ray diffraction (XRD) patterns (a) and Fourier-transform infrared spectroscopy (FTIR) spectra (b) for MBGNs and Zn-MBGNs. The relevant peaks in (b) are discussed in the text.

measured at day 7 and reached the value 67 mg L^{-1}.

3.4. Protein adsorption

Fig. 10 shows the concentration of adsorbed BSA on MBGNs and Zn-MBGNs after 2 h and 4 h. The amount of adsorbed protein increased with time. Zn-MBGNs adsorbed a significantly higher amount of BSA with respect to MBGNs at both time points.

3.5. In vitro biocompatibility

Two different cell lines were used to evaluate the potential cytotoxicity of the synthesized particles. The effect of elution extracts obtained from MBGNs and Zn-MBGNs on the proliferation of MG-63 and MEF cells was studied by measuring cell mitochondrial activity. Relative cell viability (%) of each cell line is shown in Fig. 11. Compared to the control, elution extracts from MBGNs did not show any negative effect on the viability of MG-63 and MEF cells at the tested concentrations of 5 mg mL^{-1}, 1 mg mL^{-1} and 0.1 mg mL^{-1}. Zn-MBGNs exhibited an adverse effect on MEF cell viability at the highest concentration (5 mg mL^{-1}). At the concentrations of 1 mg mL^{-1} and 0.1 mg mL^{-1} Zn-MBGNs did not show any negative effect. In case of MG-63 cells, elution extracts at all concentrations did not show any adverse effect and a significantly increased viability of MG-63 cells was observed (5 mg mL^{-1} and 1 mg mL^{-1}).

4. Discussion

In this study, mesoporous bioactive glass nanoparticles were synthesized via microemulsion assisted sol-gel method in a water-ethyl acetate-ammonia system. Cetyltrimethylammonium bromide (CTAB) was used as a surfactant and acted as a template during the hydrolysis and polycondensation of the silica precursor, which took place inside in droplets that serve as a reactor. With this approach, particles with the required dispersity and homogenous composition could be produced. On the other hand, the particles may vary in size due to the fusion and deformation of soft droplets [9]. To improve the biological behaviour of mesoporous bioactive glasses (MBGs), biologically active metallic ions are often included [15–18,30,32]. However, the addition of metal ion precursors (usually salts) may destabilize the nanoparticles by affecting condensation and changing their surface charge [33,34–36]. The proper control of processing parameters, such as the addition timing of metallic precursor [37] and the molar concentration ratio between silica and metal ion precursor [35], is necessary.

In this work, the SiO_2–CaO–ZnO system was synthesized. Zn^{2+}-free glasses (MBGNs) and Zn^{2+}-doped glasses (Zn-MBGNs) were prepared. SEM images (Fig. 1a–d) show the spherical (ovoidal) shape of particles with a size in the range of 130 ± 10 nm, which agrees with the morphology of nanoparticles synthesized using the similar method reported in the literature [25,30]. The particles were well dispersed and, importantly, the addition of zinc precursors did not affect the morphology of particles. The motivation to develop Zn^{2+}-containing MBG particles was to gain nanoparticles with therapeutic content of zinc and with a mesoporous structure, that can be additionally loaded with drugs or other therapeutic molecules. SEM analyses revealed a porous texture on

Table 2
Textural properties of the synthesized nanoparticles. S_{BET}: specific surface area; V_P: pore volume; D_P: pore diameter.

BG powders	S_{BET} (m^2/g)	V_P (cm^3/g)	$D_{P\ (nm)}$
MBGNs	229	0.29	3.71
Zn-MBGNs	274	0.28	3.72

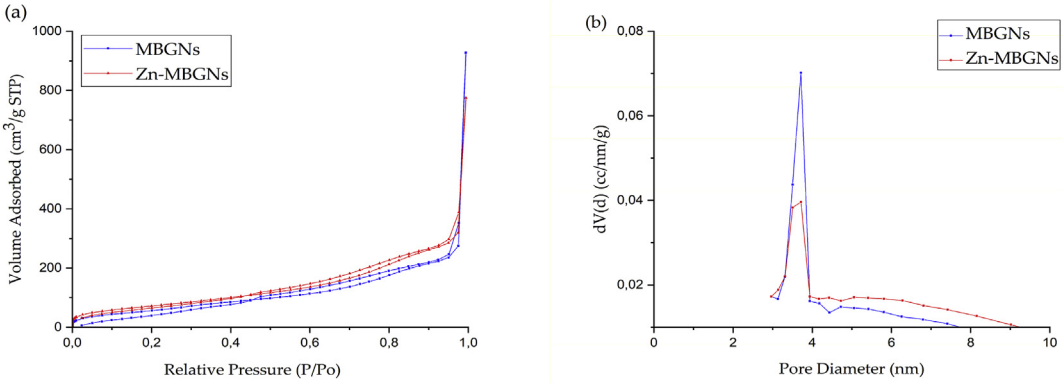

Fig. 4. N_2 adsorption-desorption isotherms (a) and pore size distribution (b) of MBGNs and Zn-MBGNs.

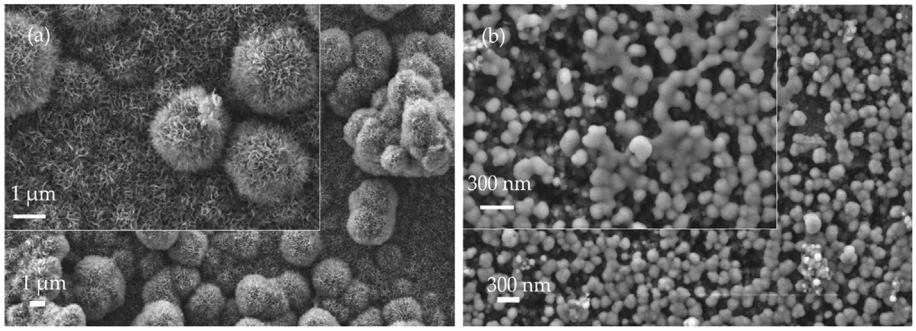

Fig. 5. SEM images showing the morphology of MBGNs (a) and Zn-MBGNs (b) soaked in SBF for 7 days.

the surface of both synthesized particles. Nitrogen adsorption analyses proved the mesoporous structure of particles. According to the International Union of Pure and Applied Chemistry (IUPAC), the nitrogen adsorption/desorption curves are type IV isotherms most similar to a type H1 hysteresis loop, specific for cylindrical open pores [11]. Although the isotherms of MBGNs and Zn-MBGNs appeared to be similar, higher gas volume was adsorbed by Zn-MBGNs. The specific surface area obtained by the Brunauer-Emmet-Teller method (BET) is 274 $m^2 g^{-1}$ for Zn-MBGNs in comparison to 229 $m^2 g^{-1}$ in the case of MBGNs. Obtained results confirmed the assertion of Lao et al. [38], that addition of zinc precursor enlarges the specific surface area in a mesoporous glass of the binary composition. The total pore volume (VP) slightly decreased from 0.29 $cm^3 g^{-1}$ (MBGNs) to 0.28 $cm^3 g^{-1}$ (Zn-MBGNs) what corresponds with increased BET of Zn-MBGNs. The diameter of the pores (DP) is identical for both proposed materials (3.7 nm), which is in the range of 2 nm–50 nm, defined as mesopores [11]. The results demonstrate that doping with Zn^{2+} did not significantly change the textural properties of the studied glasses. The lower pore volume and smaller diameter of the pores could be explained by higher contents of SiO_2 and a lower percentage of CaO in the structure of the glasses [10]. In the context of the morphological characterization, qualitative (EDX) and quantitative compositional analyses (XRF, ICP-OES) were performed. EDX spectra confirmed the presence of Si, Ca and Zn ions. The quantity of mentioned elements in the form of oxides is shown in Table 1., which summarizes data obtained by XRF and ICP-OES analyses of decomposed glasses. The nominal composition differs from the final composition. It is important to mention that washing steps conducted during the microemulsion assisted sol-gel synthesis can cause that the final composition varies from the initially calculated [32]. The glasses are XRD amorphous (Fig. 3a), demonstrated by the single broad diffused peak in the wide range of 20°–34° (2Θ) instead of high intensity narrower peaks, typical for crystalline materials. The XRD patterns did not show any peak related to Zn^{2+} based crystals, e.g. ZnO, which confirms that Zn^{2+} has been incorporated in the glass structure [32]. The molecular structure of the proposed materials was determined by FTIR (Fig. 3b). The presence of Si–O–Si stretching vibrations in the range 1000–1200 cm^{-1} and Si–O–Si bending vibration at 800 cm^{-1}, as well as Si–O–Si rocking vibration near 470 cm^{-1} were observed in both samples. The IR spectra are typical for sol-gel derived glasses [39] and no significant differences between MBGNs and Zn-MBGNs are apparent. All the above results indicate that zinc-doping did not influence the structure of the MBGNs. Further studies such as Nuclear Magnetic Resonance (NMR) and Small-Angle X-ray Scattering (SAXS) will be helpful to determine the role of Zn in the glass network.

As observed in Fig. 5, SEM analyses show differences in the morphology and textural properties of materials after immersion in SBF. On the surface of MBGNs a layer with a specific structure was visible, which indicates the formation of hydroxyapatite [40]. At the beginning, crystals were formed around the particles (day 3) and later after 7 days of immersion in SBF, the whole surface of MBGNs powder was completely covered with spherical particulates exhibiting needle-like crystals. These crystals were previously described as hydroxycarbonate apatite crystals by Kozon et al. [34], Zheng et al. [35,37,39,41] and Nawaz et al. [32]. The shape of crystals, which is not the typically cauliflower-like shape of HCAp crystals found after exposure of bioactive materials to SBF, is explained as being the consequence of the very small size of the BG particles. SEM analysis of Zn-MBGNs did not confirm the presence of HCAp crystals during the whole immersion period in SBF.

XRD and FTIR results confirm the HCAp formation only for MBGNs nanoparticles. Fig. 7 displays the presence of a sharp diffraction peak at

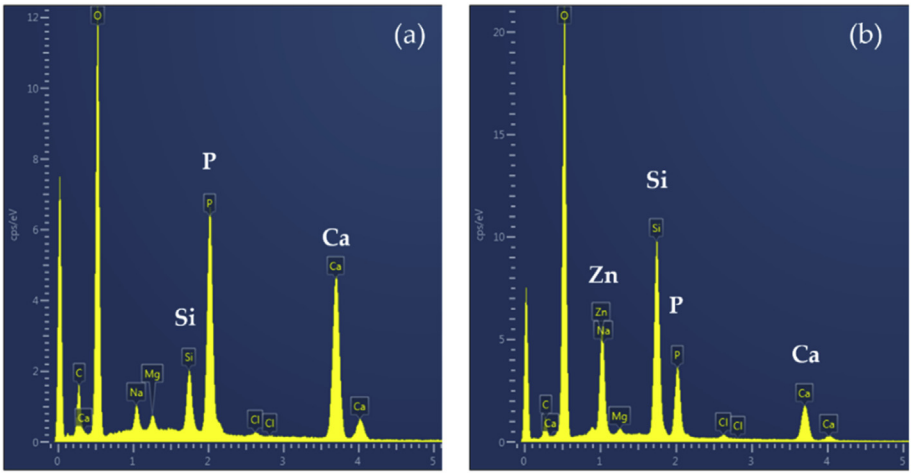

Fig. 6. EDX analysis showing the changes in elemental composition of MBGNs (a) and Zn-MBGs (b) after immersion in SBF for 7 days.

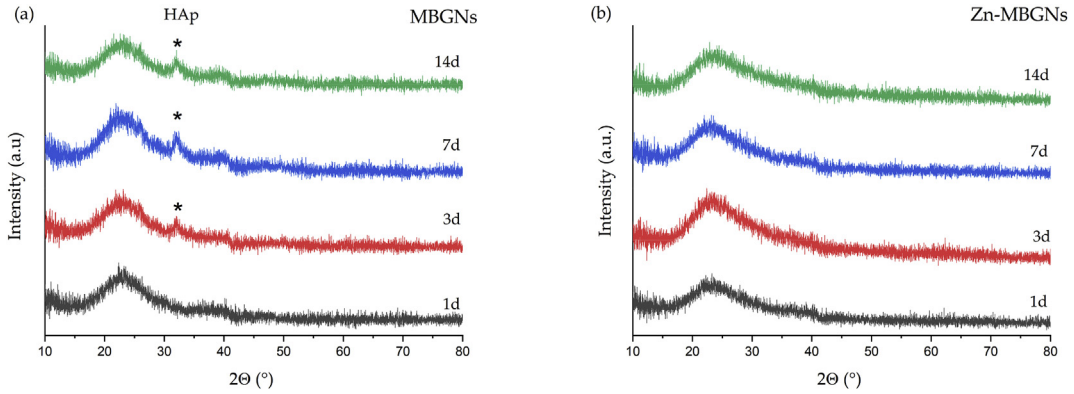

Fig. 7. X-ray diffraction (XRD) spectra of MBGNs (a) and Zn-MBGNs (b) upon immersion in SBF after 1, 3, 7 and 14 days.

32° (2Θ) identical with the XRD pattern of crystalline hydroxyapatite (JCPDS 72–1243), which started to be visible after 3 days of immersion in SBF for MBGNs. XRD spectra of Zn-MBGNs demonstrated the amorphous nature of the material during the whole immersion period. In order to fully characterize the formation of HCAp, FTIR was used. IR spectra (Fig. 8) showed the presence of a band in the region around 600 cm^{-1} corresponding to amorphous calcium phosphate and the split of this band at 560 and 603 cm^{-1} could be attributed to P–O asymmetric banding in apatite crystals [30]. The presence of these bands is visible upon 3 days of immersion in SBF but only for MBG nanoparticles. Based on all above facts, it can be concluded that the synthesized MBGNs are bioactive upon 3 days of immersion in SBF, however, Zn-MBGNs seem to be not bioactive even after 14 days of immersion in SBF. It is well known, that zinc has a great influence on the kinetics of HCAp formation [18]. As Kanzaki et al. [42] described, zinc retards crystal nucleation and inhibits crystallization because zinc ions are adsorbed at the active growth sites of HCAp and decelerate its growth during the initial period of *in vitro* mineralization in SBF. In aqueous solution PO_4^{3-} ions combine more rapidly with Zn^{2+} and create calcium zinc phosphate, unable to crystallize as HCAp [43]. Based on these facts, the deposition rate of HCAp decreased with increasing content of Zn^{2+} [18]. Despite these assertions, zinc-doped biomaterials are able to form HCAp crystal phase after longer periods of immersion [16,22,40,41]. Zheng et al. [13] reported no significant formation of HCAp in ZnO-BGN upon immersion in SBF for 14 days but confirmed HCAp formation after 21 days. Based on these facts, it can be supposed that bioactivity of Zn-MBGNs will be observed after longer immersion periods. Also, the solution conditions selected for bioactivity test significantly affected HCAp formation. Conditions such as pH adjustment and refreshment of SBF could lead to different rates of HCAp formation [44].

Fig. 9 shows the release of Zn^{2+}, Ca^{2+} and Si^{4+} ions upon soaking in SBF for 14 days. Zn-MBGNs released a relatively low amount of zinc (0.6–1.2 mg L^{-1}), which increased with time. No burst release was observed, a stable and sustained release of Zn^{2+} ions was seen. The value of leached Zn^{2+} ions corresponds to the values published by Jaroch et al. [45]. Interestingly, the material containing a relatively high amount of ZnO (~8 mol%) can release it in lower concentrations. This fact could prevent cytotoxic effect and ensure the gradual and sustained release of zinc ions in body fluids in *in vivo* conditions. The release profile suggests that Zn^{2+} is trapped in the silica network. The possibility that the limited release of zinc ions might be caused by the saturation of zinc ions in SBF cannot be strictly ruled out. However Zn^{2+} saturation in SBF is unlikely as an increasing concentration of Zn ions is visible during the whole immersion period (0.6–1.2 mg L-1). From the ion releasing profile is apparent that a higher zinc content decreased the leaching of Si^{4+}, which is consistent with the statement of Douglas et al. [46]. Zinc as a doping element in synthesized glasses delays the breakdown of the silica network [38] and increases the stability of the glasses [47]. The release profile of MBGNs demonstrated that Ca^{2+} ions were rapidly available for the reaction with PO_4^{3-} present in SBF, to create a calcium phosphate surface reaction layer. The decreasing amount of Ca^{2+} ions in SBF from day 3 corresponds with obtained results from SEM, XRD, FTIR and confirmed the formation of the HCAp layer with high content of Ca. Zn-MBGNs released Ca^{2+} ions slowly in comparison to MBGNs, which is related to the higher stability of Zn-MBGNs. On the other hand, the amount of released Ca^{2+} ions present in SBF was higher compared with MBGNs. This is attributed to the retarded formation of HCAp by Zn-MBGNs. The release profile of Zn^{2+}, Ca^{2+} and Si^{4+} ions indicate that the synthesized MBGNs and Zn-MBGNs are degradable, thereby fulfilling the necessary feature of biomaterials for tissue engineering applications.

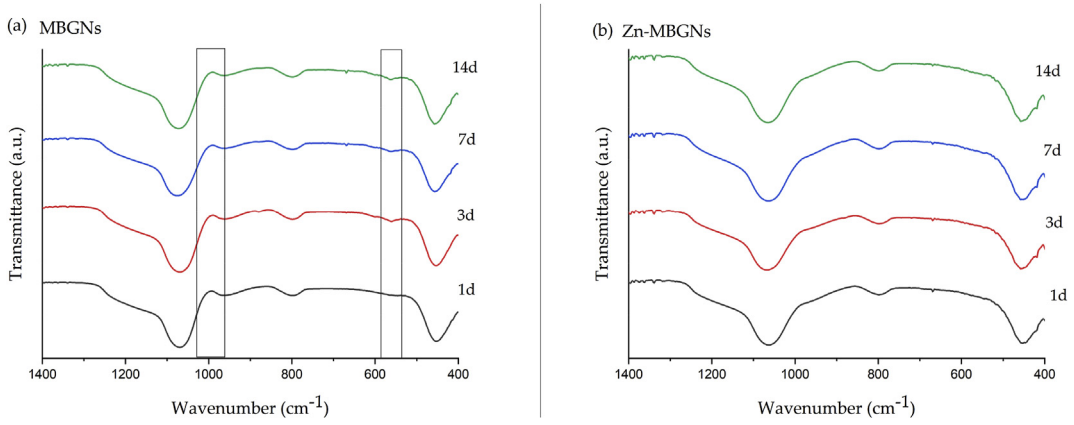

Fig. 8. FTIR spectra of MBGNs (a) and Zn-MBGNs (b) after immersion in SBF for 1, 3, 7 and 14 days.

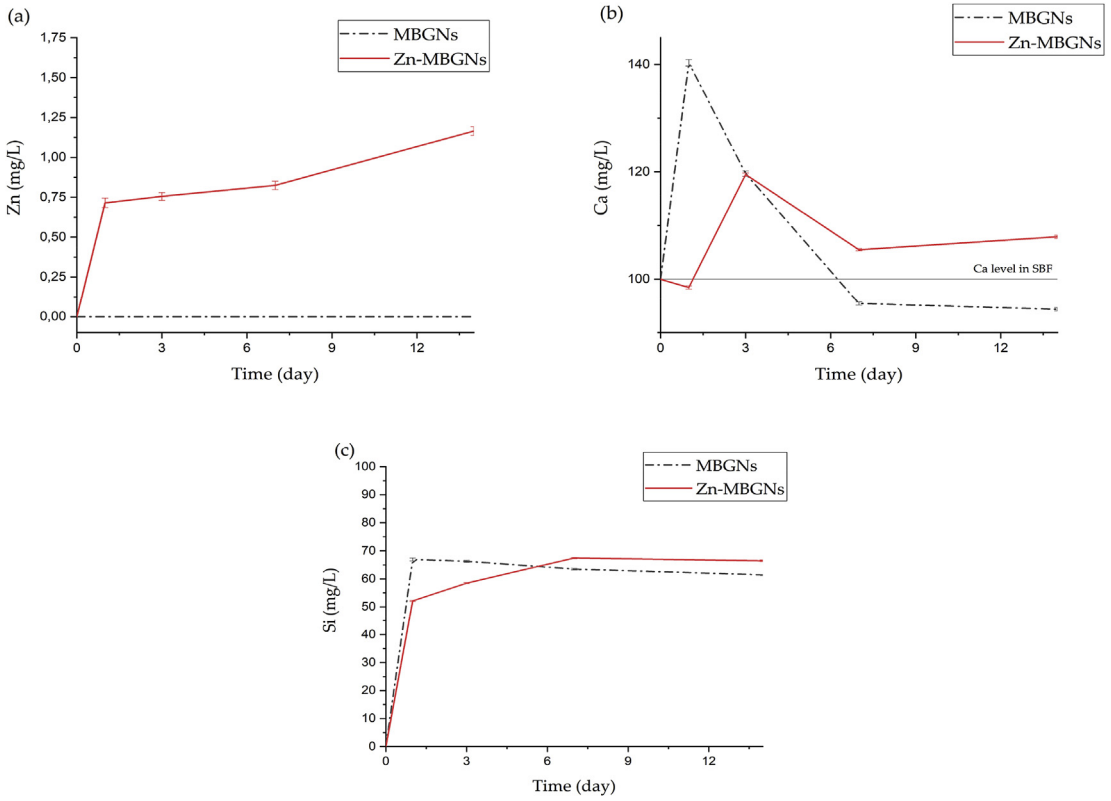

Fig. 9. Ions release profile of MBGNs and Zn-MBGNs determined by optical emission spectroscopy with inductively coupled plasma (ICP-OES). The concentration of Zn^{2+} (a), Ca^{2+} (b) and Si^{4+} (c) in SBF for 1, 3, 7 and 14 days.

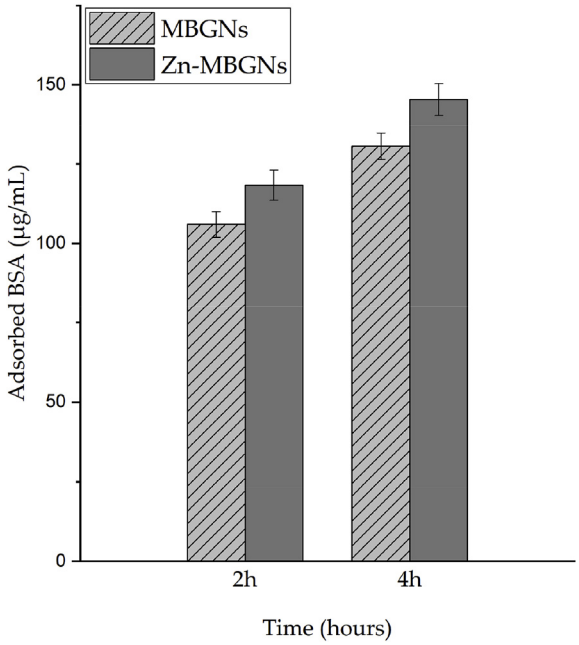

Fig. 10. Adsorption of bovine serum albumin (BSA; µg mL^{-1}) on the surface of MBGNs and Zn-MBGNs nanoparticles.

Implanted biomaterials come to contact with blood or body fluids immediately after implantation. The proteins from the surrounding environments are spontaneously adsorbed on to the host surface in a short time [48]. Adsorbed proteins represent the primary steps for later cellular attachment and afterwards proliferation and migration of cells [48–50]. Stronger adsorption of proteins to the surface of the proposed material could predict successful attachment of cells under *in vivo* conditions [51]. In the case of mesoporous material, it is important to mention that the passive adsorption of proteins on the surface is the most commonly used approach in drug delivery applications [52]. In this study, the both glasses exhibit ability to adsorb proteins (Fig. 10). However, Zn-MBGNs adsorbed a higher amount of BSA (145 µg mL^{-1}) in comparison to MBGNs (131 µg mL^{-1}). Dee et al. [51] stated that the surface topography beside other parameters, is a crucial precondition influencing adsorption of proteins. The roughness, porosity, pore size and size of the particles determine the surface area which interacts with proteins [51]. Based on the mentioned facts, the higher surface area (274 $m^2 g^{-1}$) for Zn-MBGNs in comparison to 229 $m^2 g^{-1}$ for MBGs is likely the reason for the higher protein adsorption [53].

The possible toxic effect of zinc on cells was discussed in the work of Aina et al. [54] and Haimi et al. [55]. In the case of BGs, doping with ~5 mol% is considered to be the boundary content of zinc without showing cytotoxicity [16,17,54–56]. Elution extracts obtained from Zn-MBGNs exhibited adverse effects only on the growth of MEF cells at the highest concentration (5 mg mL^{-1}). Other concentrations did not negatively affect the growth of the studied cell lines (Fig. 11). In this study, Zn-MBGNs (~8 mol% of ZnO) did not show cytotoxic effect towards osteoblast-like cells (MG-63) and embryonic fibroblasts (MEF). This result can be explained considering the relatively low concentration of Zn^{2+} ions released into the medium (1.2 mg L^{-1} = 1.2 ppm; value obtained from ICP test). However it is necessary to consider also the potential variation in release profile by utilizing different media e.g. SBF, DMEM, RPMI, etc. Studies of ion release into different media investigating also the effects of solution conditions (pH, protein presence) are necessary and remain a task for future research. However, released amount of Zn^{2+} demonstrates the supportive effect on the growth and proliferation of osteoblast-like cells in dose depending manner. The concentration of Zn^{2+} in human plasma varies from 0.73 to 1.73 ppm, with the mean value of 1 mg L^{-1} [57]. Aina et al. [54] reported high proliferation of endothelial cells at Zn^{2+} concentration of 1.1 ppm. In

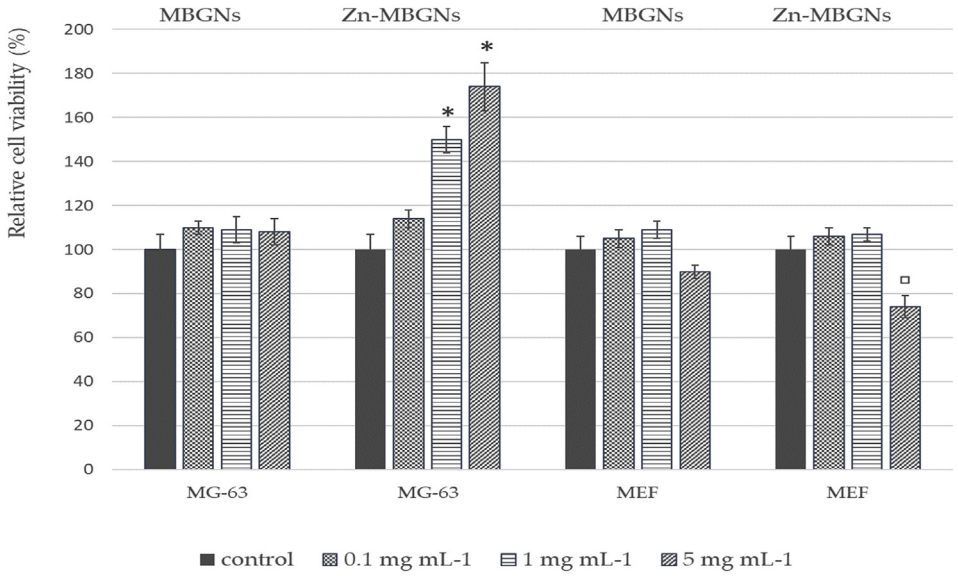

Fig. 11. Quantitation of viable cells number of MG-63 and MEF cells in cytotoxicity assay towards MBGNs and Zn-MBGNs elution extracts at 0.1 mg mL^{-1}, 1 mg mL^{-1} and 5 mg mL^{-1} concentration. * ($p < 0.05$) significant increase respect to the control; ▫ ($p < 0.05$) significant decrease respect to the control.

the same study, 2.7 ppm concentration was described as toxic. Balamurugan et al. [58] confirmed the enhanced proliferation and differentiation of osteoblast cells promoted by zinc-substituted BGs. In the same way, Salinas et al. [17] described the osteogenic effect of zinc-doped BGs in pre-osteoblastic cell culture. However, Haimi et al. [55] published results which did not support the osteogenic effect of zinc-doped BG. These contradictory statements are most likely caused by the different ability of the glasses to release Zn^{2+} ions to the culture media. This fact is also discussed by Zheng et al. [13] describing the osteogenic effect of zinc modified BG on mesenchymal stem cells, already at concentration of 0.95 mg L^{-1}. It is important to take into account the presence of other elements in the glass and finally also the synergistic effect of different dissolution products.

Although a rapid apatite forming ability of BG benefits their use in bone repair/regeneration, in some biomedical applications, e.g. soft tissue regeneration and especially in the wound healing area, the mineralization of BG is not necessary and even not desired as the formation of apatite could retard the release of therapeutic ions [22], for example Zn^{2+} ions. Therefore, the developed Zn-MBG, with the ability to release active ions in a sustained manner, are also expected to be effective in wound healing and drug delivery applications.

5. Conclusions

In this study zinc-containing mesoporous bioactive glass particles were synthesized by using micro-emulsion assisted sol-gel method by employing CTAB as a surfactant. We developed well dispersed spherical particles with the size 130 ± 10 nm and ~8 mol% content of ZnO. Addition of zinc did not have influence on the amorphous structure of the glass and the textural properties, including the specific surface area, were positively affected. Obtained results confirmed reduced mineralization and delayed formation of HAp affected by the presence of Zn^{2+}. Zn-MBGNs were able of gradual, sustained release of zinc ions to the medium. Not only Zn-MBGNs did not exhibit cytotoxic effect towards osteoblast-like cells and embryonic fibroblasts, but also supported the growth of osteoblast like cells. Additionally, Zn-MBGNs demonstrated improved ability to adsorb proteins. Future work will focus on investigating the antibacterial influence of the material and possible cytotoxic effect in direct contact with Zn-MBGNs. Based on the results obtained so far, the new Zn-MBGNs are considered promising for soft tissue regeneration and wound healing application.

Author contributions

Z.N. performed the experiments, analysed the data and wrote the original draft; K.Z. performed experiments, reviewed and edited the paper; L.L. supervised the experimental work and revised the paper; D.G., H.K., Q.N., M.M. performed the experiments; D.G. organized the financial support and discussed results; A.R.B. designed and directed the project, planned the research activity, supervised the work and revised the publication. All authors provided critical feedback and corrected the paper.

Funding

This project has received funding from the European Union's Horizon 2020 research and innovation program under grant agreement No 739566 and in the frame of the project Centre for Functional and Surface Functionalized Glass (CEGLASS), ITMS code is 313011R453, operational program Research and innovation, co-funded from European Regional Development Fund. The financial support of this work by the grant VEGA 2/0026/17 and APVV 15/0014 is also gratefully acknowledged.

Declaration of competing interest

The authors declare no conflict of interest.

References

[1] J.R. Jones, Bio-Glasses: An Introduction, Wiley, 2012.
[2] F. Baino, G. Novajra, V. Miguez-Pacheco, A.R. Boccaccini, C. Vitale-Brovarone, Bioactive glasses: special applications outside the skeletal system, J. Non-Cryst. Solids 432 (2016) 15–30.
[3] F. Baino, 'Bioactive glasses – when glass science and technology meet regenerative medicine', Ceram. Int. 44 (13) (2018) 14953–14966.
[4] A.M. Alsharabasy, A mini-review on the bioactive glass-based composites in soft tissue repair, Bioceram. Dev. Appl. 8 (1) (2018) 8–11.
[5] P. Balasubramanian, T. Büttner, V. Miguez Pacheco, A.R. Boccaccini, Boron-containing bioactive glasses in bone and soft tissue engineering, J. Eur. Ceram. Soc. 38 (3) (2018) 855–869.
[6] L.L. Hench, J.M. Polak, Third-generation biomedical materials, Science 295 (5557) (2002) 1014–7.
[7] E. Fiume, J. Barberi, E. Verné, F. Baino, Bioactive glasses: from parent 45S5 composition to scaffold-assisted tissue-healing therapies, J. Funct. Biomater. 9 (1) (2018).
[8] G. Renaudin, P. Laquerriere, Y. Filinchuk, E. Jallot, J.M. Nedelec, Structural characterization of sol–gel derived Sr-substituted calcium phosphates with anti-

osteoporotic and anti-inflammatory properties, J. Mater. Chem 18 (2008) 3593–3600.
[9] K. Zheng, A.R. Boccaccini, Sol-gel processing of bioactive glass nanoparticles: a review, Adv. Colloid Interface Sci. 249 (2017) 363–373.
[10] X. Yan, C. Yu, X. Zhou, J. Tang, D. Zhao, Highly ordered mesoporous bioactive glasses with superior *in vitro* bone-forming bioactivities, Angew. Chem. Int. Ed. 43 (44) (2004) 5980–5984.
[11] A.V. Neimark, et al., Physisorption of gases, with special reference to the evaluation of surface area and pore size distribution (IUPAC Technical Report), Pure Appl. Chem. 87 (9–10) (2015) 1051–1069.
[12] R. Narayan, U.Y. Nayak, A.M. Raichur, S. Garg, Mesoporous silica nanoparticles: a comprehensive review on synthesis and recent advances, Pharmaceutics 10 (3) (2018) 1–49.
[13] K. Zheng, et al., ZnO quantum dots modified bioactive glass nanoparticles with pH-sensitive release of Zn ions, fluorescence, antibacterial and osteogenic properties, J. Mater. Chem. B 4 (48) (2016) 7936–7949.
[14] Z. Hong, W.J. Stark, A.R. Boccaccini, D. Mohn, J.F. Mano, M. Erol, Polymer/bioactive glass nanocomposites for biomedical applications: a review, Compos. Sci. Technol. 70 (13) (2010) 1764–1776.
[15] C. Wu, J. Chang, Multifunctional mesoporous bioactive glasses for effective delivery of therapeutic ions and drug/growth factors, J. Control. Release 193 (2014) 282–295.
[16] S. Sánchez-Salcedo, S. Shruti, A.J. Salinas, G. Malavasi, L. Menabue, M. Vallet-Regí, *In vitro* antibacterial capacity and cytocompatibility of SiO 2-CaO-P2O5 mesо-macroporous glass scaffolds enriched with ZnO, J. Mater. Chem. B 2 (30) (2014) 4836–4847.
[17] A. Salinas, et al., Osteogenic effect of ZnO-mesoporous glasses loaded with osteostatin, Nanomaterials 8 (8) (2018) 592.
[18] P. Balasubramanian, L.A. Strobel, U. Kneser, A.R. Boccaccini, Zinc-containing bioactive glasses for bone regeneration, dental and orthopedic applications, Biomed. Glass 1 (1) (2015) 51–69.
[19] C.T. Chasapis, C.A. Spiliopoulou, A.C. Loutsidou, M.E. Stefanidou, Zinc and human health: an update, Arch. Toxicol. 86 (4) (2012) 521–534.
[20] M. Stefanidou, C. Maravelias, A. Dona, C. Spiliopoulou, Zinc: a multipurpose trace element, Arch. Toxicol. 80 (1) (2006) 1–9.
[21] N. Stubbs, A.B.G. Lansdown, M.S. Ågren, U. Mirastschijski, E. Scanlon, Zinc in wound healing: theoretical, experimental, and clinical aspects, Wound Repair Regen. 15 (1) (2007) 2–16.
[22] S. Naseri, W.C. Lepry, S.N. Nazhat, Bioactive glasses in wound healing: hope or hype? J. Mater. Chem. B 5 (31) (2017) 6167–6174.
[23] S. Shruti, M. Vallet-Regí, L. Menabue, G. Malavasi, A.J. Salinas, Substitutions of cerium, gallium and zinc in ordered mesoporous bioactive glasses, Acta Biomater. 7 (9) (2011) 3452–3458.
[24] S. Shruti, A.J. Salinas, G. Lusvardi, G. Malavasi, L. Menabue, M. Vallet-Regi, Mesoporous bioactive scaffolds prepared with cerium-, gallium- and zinc-containing glasses, Acta Biomater. 9 (1) (2013) 4836–4844.
[25] Y.F. Goh, A.Z. Alshemary, M. Akram, M.R. Abdul Kadir, R. Hussain, *In vitro* study of nano-sized zinc doped bioactive glass, Mater. Chem. Phys. 137 (3) (2013) 1031–1038.
[26] Q. Liang, Q. Hu, G. Miao, B. Yuan, X. Chen, A facile synthesis of novel mesoporous bioactive glass nanoparticles with various morphologies and tunable mesostructure by sacrificial liquid template method, Mater. Lett. 148 (2015) 45–49.
[27] T. Kokubo, H. Takadama, How useful is SBF in predicting in vivo bone bioactivity? Biomaterials 27 (15) (2006) 2907–2915.
[28] R.F. Wallin, P.J. Upman, A practical guide to ISO 10993, Medical Device and Diagnostic Industry Magazine, 1998 http://www.devicelink.com/mddi/archive/98/01/023.h.
[29] K. Zheng, et al., Towards highly dispersed mesoporous bioactive glass nanoparticles with high Cu concentration using Cu/ascorbic acid complex as precursor, Front. Chem. 7 (2019) 497.
[30] J.M. Hughes, Structure and Chemistry of the apatites and other calcium orthophosphates by, 1994. xii + 389 pp. ISBN 0-444-81582-1.', J. Am. Chem. Soc. in: J.C. Elliot (Ed.), The London Hospital Medical College, vol 118, Elsevier, Amsterdam, Jan. 1996, p. 3072 12.
[31] K. Zheng, et al., Aging time and temperature effects on the structure and bioactivity of gel-derived 45S5 glass-ceramics, J. Am. Ceram. Soc. 98 (1) (2014) 30–38.
[32] Q. Nawaz, et al., Synthesis and characterization of manganese containing mesoporous bioactive glass nanoparticles for biomedical applications, J. Mater. Sci. Mater. Med. 29 (5) (2018).
[33] M. Taherian, R. Rojaee, M. Fathi, M. Tamizifar, Effect of different sol-gel synthesis processes on microstructural and morphological characteristics of hydroxyapatite-bioactive glass composite nanopowders, J. Adv. Ceram. 3 (3) (2014) 207–214.
[34] E. Boccardi, D. Kozon, K. Zheng, Y. Liu, L. Liverani, A.R. Boccaccini, Synthesis of monodispersed Ag-doped bioactive glass nanoparticles via surface modification, Materials (Basel) 9 (4) (2016) 225.
[35] O. Tsigkou, S. Labbaf, M.M. Stevens, A.E. Porter, J.R. Jones, Monodispersed bioactive glass submicron particles and their effect on bone marrow and adipose tissue-derived stem cells, Adv. Healthc. Mater. 3 (1) (2014) 115–125.
[36] S.L. Greasley, et al., Controlling particle size in the Stöber process and incorporation of calcium, J. Colloid Interface Sci. 469 (2016) 213–223.
[37] K. Zheng, et al., Timing of calcium nitrate addition affects morphology, dispersity and composition of bioactive glass nanoparticles, RSC Adv. 6 (97) (2016) 95101–95111.
[38] L. Courthéoux, et al., Controlled Bioactivity in Zinc-Doped Sol − Gel-Derived Binary Bioactive Glasses, J. Phys. Chem. C 112 (2008) 13663–13667.
[39] H. Aguiar, P. González, J. Serra, Bioactive glass structure and solubility, Bioactive Glasses, second ed., 2018, pp. 37–61.
[40] T. Kasuga, Y. Hosoi, M. Nogami, M. Niinomi, Apatite formation on calcium phosphate invert glasses in simulated body fluid, J. Am. Ceram. Soc. 84 (2) (2001) 450–452.
[41] K. Zheng, X. Dai, M. Lu, N. Hüser, N. Taccardi, A.R. Boccaccini, Synthesis of copper-containing bioactive glass nanoparticles using a modified Stöber method for biomedical applications, Colloids Surfaces B Biointerfaces 150 (2017) 159–167.
[42] N. Kanzaki, K. Onuma, G. Treboux, S. Tsutsumi, A. Ito, Inhibitory effect of magnesium and zinc on crystallization kinetics of hydroxyapatite (0001) face, J. Phys. Chem. B 104 (17) (2000) 4189–4194.
[43] R.L. Du, J. Chang, S.Y. Ni, W.Y. Zhai, J.Y. Wang, Characterization and *in vitro* bioactivity of zinc-containing bioactive glass and glass-ceramics, J. Biomater. Appl. 20 (4) (2006) 341–360.
[44] X. Lu, J. Kolzow, R.R. Chen, J. Du, Effect of solution condition on hydroxyapatite formation in evaluating bioactivity of B2O3 containing 45S5 bioactive glasses, Bioact. Mater. 4 (May) (2019) 207–214.
[45] D.B. Jaroch, D.C. Clupper, 'Modulation of zinc release from bioactive sol–gel derived SiO2-CaO-ZnO glasses and ceramics', J. Biomed. Mater. Res. A 82A (3) (2007) 575–588.
[46] R.W. Douglas, T.M.M. El-Shamy, Reactions of glasses with aqueous solutions, J. Am. Ceram. Soc. 50 (1) (Jan. 1967) 1–8.
[47] C. Soundrapandian, A. Mahato, B. Kundu, S. Datta, B. Sa, D. Basu, Development and effect of different bioactive silicate glass scaffolds: *in vitro* evaluation for use as a bone drug delivery system, J. Mech. Behav. Biomed. Mater. 40 (2014) 1–12.
[48] F. Muhammad, et al., PH-triggered controlled drug release from mesoporous silica nanoparticles via intracellular dissolution of ZnO nanolids, J. Am. Chem. Soc. 133 (23) (2011) 8778–8781.
[49] A. Laczka-Osyczka, M. Laczka, S. Kasugai, K. Ohya, Behavior of bone marrow cells cultured on three different coatings of gel-derived bioactive glass-ceramics at early stages of cell differentiation, J. Biomed. Mater. Res. 42 (3) (1998) 433–442.
[50] D.A. Puleo, A. Nanci, Understanding and controlling the bone-implant interface, Biomaterials 20 (23–24) (1999) 2311–2321.
[51] K.C. Dee, D.A. Puleo, R. Bizios, C.J. Wiley, K.C. Dee, D. Ph, Tissue- Biomaterial Interactions an Introduction to Tissue- Biomaterial Interactions vol 4, (2002).
[52] W.C. Liu, B. Ballenger, A. Algarni, M. Velez, T.-M. Chu, FTIR Characterization and Release of Bovine Serum Albumin from Bioactive Glasses vol 15, (2017).
[53] K. Zheng, M. Kapp, A.R. Boccaccini, Protein interactions with bioactive glass surfaces: a review, Appl. Mater. Today 15 (2019) 350–371.
[54] A. Fiorio Pla, L. Munaron, C. Morterra, V. Aina, G. Malavasi, Zinc-containing bioactive glasses: surface reactivity and behaviour towards endothelial cells, Acta Biomater. 5 (4) (2008) 1211–1222.
[55] S. Haimi, et al., Characterization of zinc-releasing three-dimensional bioactive glass scaffolds and their effect on human adipose stem cell proliferation and osteogenic differentiation, Acta Biomater. 5 (8) (2009) 3122–3131.
[56] V. Salih, A. Patel, J.C. Knowles, Zinc-containing phosphate-based glasses for tissue engineering, Biomed. Mater. 2 (1) (Mar. 2007) 11–20.
[57] K. Kaur, R. Gupta, S.A. Saraf, S.K. Saraf, Zinc: the metal of life, Compr. Rev. Food Sci. Food Saf. 13 (4) (2014) 358–376.
[58] A. Balamurugan, G. Balossier, S. Kannan, J. Michel, A.H.S. Rebelo, J.M.F. Ferreira, 'Development and *in vitro* characterization of sol–gel derived CaO–P2O5–SiO2–ZnO bioglass', Acta Biomater. 3 (2) (2007) 255–262.